The carbonaceous dust at sub-parsec scales in the nucleus of NGC 1068

Violeta Gámez Rosas, Alexander Tielens, Paul van der Werf, Walter Jaffe, James Leftley, Leonard Burtscher, Romain Petrov, Jacob Isbell, Bruno López, Florentin Millour, et al.

Monthly Notices of the ROYAL ASTRONOMICAL SOCIETY

MNRAS **525,** 1142–1152 (2023) https://doi.org/10.1093/mnras/stad2233
Advance Access publication 2023 July 29

The carbonaceous dust at sub-parsec scales in the nucleus of NGC 1068

Violeta Gámez Rosas [1]★ Alexander G. G. M. Tielens,[1]★ Paul van der Werf,[1]★ Walter Jaffe,[1]★ James H. Leftley,[2] Leonard Burtscher,[1] Romain Petrov,[2] Jacob W. Isbell,[3] Bruno López,[2] Florentin Millour,[2] Anthony Meilland,[2] Alexis Matter,[2] Laurens B. F. M. Waters[4,5] and Klaus Meisenheimer[3]

[1]*Sterrewacht Leiden, Niels Bohrweg 2, 2333 CA Leiden, The Netherlands*
[2]*Laboratoire Lagrange, Université Côte d'Azur, Observatoire de la Côte d'Azur, CNRS, Boulevard de l'Observatoire, CS 34229, 06304 Nice Cedex 4, France*
[3]*Max-Planck-Insitut für Astronomie, Königstuhl 17, 69117 Heidelberg, Germany*
[4]*Department of Astrophysics, Radboud University, Heyendaalseweg 135, 6525 AJ Nijmegen, The Netherlands*
[5]*SRON, Niels Bohrweg 4, 2333 CA Leiden, The Netherlands*

Accepted 2023 July 17. Received 2023 July 7; in original form 2022 July 15

ABSTRACT

Single dish observations of NGC 1068 have shown the presence of a 3.4 μm aliphatic hydrocarbon absorption feature similar to diffuse lines of sight towards the Galactic Centre. Both, the single dish spectra and the correlated fluxes obtained by MATISSE, present a broad absorption profile in the L band as well, that vary from baseline to baseline. A new CRIRES spectrum with a slit width comparable to the MATISSE aperture also reveals a wide feature around 3.4 μm. We aim to analyse these features to learn about their origin and the distribution of the carriers across the source. We argue that all these features are caused by absorption of aliphatic hydrocarbons. The 3.4 μm absorption features in the interferometric MATISSE correlated fluxes vary in optical depth over scales of 0.2-1.4 parsec in the plane of the sky, although probably placed at a larger distance from the AGN along the line of sight. The absorption in the extended areas seems to peak in the direction of the inner jet, close to the center of the ionization cone. These results support the theory of a clumpy torus. In comparing our results to the N-band surface density previously reported, we have discovered a mass ratio of carbonaceous to silicate olivine dust at ∼2 - 3.6 per cent, which is similar to those found in several lines of sight in the diffuse interstellar medium of our Galaxy.

Key words: instrumentation: interferometers – galaxies: active – galaxies: nuclei – galaxies: Seyfert – galaxies: NCG 1068: ISM – infrared: diffuse background.

1 INTRODUCTION

Many lines and features observed in infrared L-band (2.8–4.0 μm) spectra of astronomical sources are valuable diagnostics for the physical and chemical conditions of the gas and dust in these sources. These lines include the hydrogen recombination lines (Pf δ at 3.29 μm, Pf γ at 3.74 μm and Br α at 4.05 μm), water ice absorption at 3.08 μm, aromatic hydrocarbons at 3.28 μm, aliphatic hydrocarbons at $\sim$ 3.4 μm or nanodiamond features at $\sim$ 3.5 μm. In particular, PAHs and aliphatic hydrocarbon features are easily recognised in low spectral resolution observations, such as those presented in this paper.

The 3.4 μm carbonaceous dust absorption feature has been detected through several lines of sight towards the Galactic centre probing the diffuse interstellar medium (DISM) (Sandford et al. 1991; Pendleton et al. 1994; Chiar et al. 2000, 2002). It has also been observed in planetary nebulae and in the spectra of meteorites (Ehrenfreund et al. 1991; Chiar et al. 1998). In the case of extra-galactic objects, the first detection of this feature was done in NGC 1068, and since then, it has been extensively studied (Imanishi et al. 1997; Tomono et al. 2001; Dartois et al. 2004; Tomono, Terada & Kobayashi 2006; Geballe et al. 2009). Furthermore, the feature has been observed in several other AGNs and ULIRGs (Dartois et al. 2004; 2007; Mason et al. 2004; Imanishi, Dudley & Maloney 2006). There has been much progress to explain the origin of this feature (which has been found also in emission) attributed to the aliphatic C-H stretch in carbonaceous dust (Sandford et al. 1991; Pendleton & Allamandola 2002; Chiar et al. 2013; 2021; Günay et al. 2018, 2020). Spectropolarimetry of the feature in the DISM showed that the silicate grains that cause the broad feature at ∼9.7 μm and the carbon grains that carry the hydrocarbons are actually independent but co-spatial populations (Chiar et al. 2006).

Recently, Gámez Rosas et al. (2022) reported the detection of a feature in the long baseline L-band inteferometry of NGC 1068 at an unprecedented angular resolution (∼3 milliarcsec) that vary with baseline length and baseline position angle. In this work, we analyse

★ E-mail: gamez@strw.leidenuniv.nl (VGR); tielens@strw.leidenuniv.nl (AGGMT); pvdwerf@strw.leidenuniv.nl (PVDW); jaffe@strw.leidenuniv.nl (WJ)
∗ ESO programmes 60.A-9257 (commissioning) and 0104.B-0322(A) (MATISSE Guaranteed Time Observations of AGNs). For a table with observations of the science target and calibrators with the conditions during the observations see A1.

these features and study their spatial distribution on subparsec scales by means of geometric models. We also calculate the fraction of the carbon in aliphatic form for NCG 1068.

2 OBSERVATIONS, DATA REDUCTION AND CALIBRATION

2.1 MATISSE

MATISSE is an infrared spectro-interferometer located at the ESO VLT interferometer, in Cerro Paranal, Chile. It covers the L, M and N bands, from ∼3 to ∼13 μm and it can observe in low (R∼30), medium (R∼500 or 900) and high (R∼3400) spectral resolutions. It can combine the beams of four telescopes at a time, the Auxiliary Telescopes (ATs, diameters of 1.8 m) or the Unit Telescopes (UTs, with diameters of 8 m), and generate closure phases which do not carry the errors in the phases that are introduced by the atmospheric variations. This is essential to keep the information on the morphology of the emitting sources. The baselines can span lengths from 20 m to up to 200 m, which makes it an ideal instrument to study the extended emission in NGC 1068 previously found by Jaffe et al. (2004) and López-Gonzaga et al. (2014) and the innermost structures resolved by Gámez Rosas et al. (2022).

The morphology of the dust emission in NGC 1068 is one of the key science goals of MATISSE (Lopez et al. 2014; 2021) therefore it was observed during one of the first commissioning rounds in 2018 September 22 and 25. We combined those observations with guaranteed time observations on 2019 November 7. They were all made with the 8.1-m telescopes (UTs) at low spectral resolution (R∼30) in the Simultaneous Photometry mode (SIPHOT, where the photometric and interferometric channels are recorded at the same time), and chopped at 0.5 Hz. The baseline lengths of these observations go from ∼40 m to ∼130 m. We obtained a total of five snapshots which from now on we will refer to as 'dates' numbered from 0 to 4, even though three of them were taken on the same night of 2019 November 7.

MATISSE uses a Beam Commuting Device (BCD) to calibrate the closure phases, and has in total four different arrangements named IN-IN, IN-OUT, OUT-IN and OUT-OUT. During commissioning, only IN-IN and OUT-OUT were used, so we make use only of those same configurations for the rest of the data. While using only IN-IN and OUT-OUT BCDs the closure phases contain residuals caused by the cross talks between the beams and baselines of a few degrees (<3 degrees, Petrov et al. (2022)), calibrating them using the four BCD arrangements can reduce these errors to a fraction of a degree. This difference is not critical for our scientific goal since NGC 1068 has phases spanning values from -180 to +180 degrees and we focus on the large scale structure of the emitting sources. Nonetheless, we calibrated the BCDs by averaging the data taken in the two modes.

The raw data that we obtain from MATISSE come in oifits files and have to undergo a 'cleaning' (subtraction of a flat field, identification of hot pixels, etc.), which is commonly called 'reduction', and a calibration process. The reduction is done by the MATISSE pipeline, separately for the science target and the calibrator stars. In this work we focus on the L band data. For the data reduction of both, target and calibrators, we used the ESO/MATISSE ESOREX Data Reduction Software (DRS) pipeline. Specifically, we used the parameters corrFlux=FALSE, OpdMod=FALSE and compensate = [pb,nl,if,rb,bp,od] for the master recipe mat_raw_estimates. The outputs of this process are uncalibrated or instrumental squared visibilities and closure phases, and an uncalibrated spectrum taken by each telescope.

To calibrate the instrumental interferometric observables (squared visibilities and closure phases) and the four single dish spectra we chose mid-IR interferometric standard stars from the catalogue Cruzalebes et al. (2019), that were at similar airmass as the target (10° from the target or closer) at the moment of the observation, within a factor 2 in flux to the target, and with small and accurate angular diameters. This calibration gets rid of any instrumental effect caused by a low flux of the source or the atmospheric transmission due to the air mass above the observatory, this is the reason why we observe the calibrator close in time and why it has to be similar in flux to the target. NGC 1068 is considered a low flux target for MATISSE, therefore this step is crucial to obtain reliable data.

To reduce the noise of the squared visibilities, and ultimately, of the correlated fluxes, we made a 'BCD calibration' of the data by taking the average of the reduced data observed in IN-IN and OUT-OUT BCD settings, for each date.

For the spectrophotometric calibration of the single dish spectra of the target we observed Cohen (Cohen et al. 1986) calibrators, with known absolute flux scales and spectral shapes from atmospheric models resulting in the spectrum in units of Jy.

Finally, to obtain the correlated fluxes we multiplied the square root of the calibrated square visibilities by the flux-calibrated photometry. A complete description of these procedures is covered with more detail in Gámez Rosas et al. (2022).

2.2 CRIRES

To obtain high spectral resolution 8-meter telescope L-band spectra of NGC 1068 we requested observations using ESO's CRIRES +, the upgraded CRyogenic high-resolution InfraRed Echelle Spectrograph instrument at the VLT (https://www.eso.org/sci/facilities/develop/instruments/crires_up.html). The full resolution data ($R \sim 80,000$) will be analyzed in a future paper, but the optical depth profiles, convolved to lower resolution, are presented in Fig. 1 for comparison with other non-interferometric spectra.

The slit of 0.2' width was centered on the nucleus and two exposures of 46 sec each were taken with the target moved 6' along the slit ('nodding') which where then subtracted to remove sky emission, and then shifted to the same position and subtracted to yield the target spectrum. Normally three such exposure pairs are necessary to cover all echelle orders, and these were taken on 2022-01-06. By a technical mistake, an additional exposure pair was taken on 2021-10-29, and this was averaged together with the corresponding data from 2022. The wavelength coverage was 2.87 μm to 4.14 μm with an effective resolution of $\simeq 80,000$. With the use of the MACAO adaptive optics system on the 8-meter Unit Telescopes of ESO's Very Large Telescope system, the effective resolution of the L-band images was 0.2. The spectra were reduced and extracted using the official CR2RE 1.2.0 pipeline. The filter shape for each observation was removed manually using the pipeline provided blaze function before being calibrated of atmospheric contamination using MOLECFIT v4.2.3. The final data product of this process was the calibrated spectrum in ADU/s. To convert to absolute flux density, we performed the same calibration on the B9V star Lambda Aquilae (m L = 3.6) taken on 2021-09-18. This early type star has a smooth continuum except for absorption features near the Hydrogen recombination lines at wavelengths of 3.04, 3.30, and 3.40 μm. In these regions the instrumental calibrator spectrum was interpolated from points outside the lines. We note that in some of the comparison spectra include in Fig. 1, this was not done, with the result that an

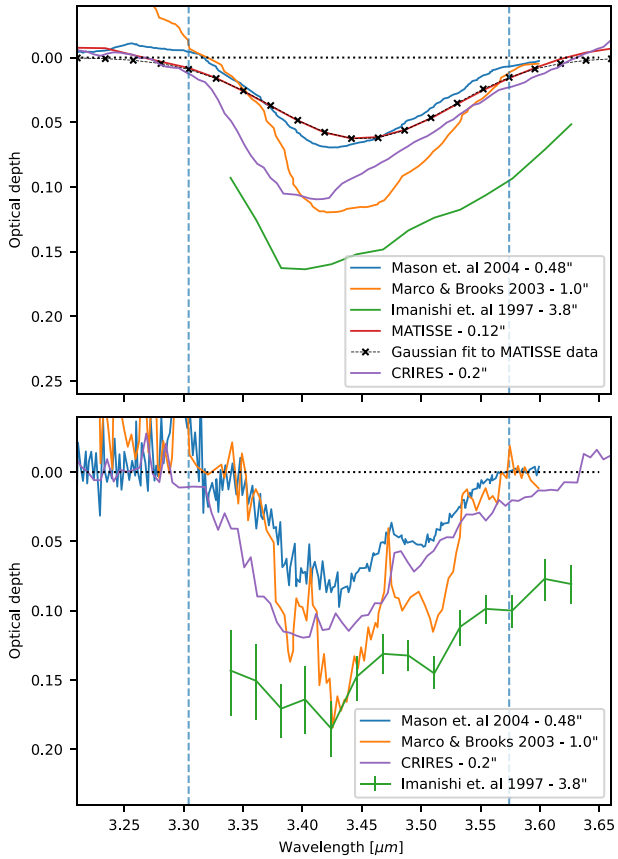

Figure 1. Top: MATISSE and CRIRES NGC 1068 continuum subtracted and normalised feature from the average single-dish photometry, compared to the optical depths from Imanishi et al. (1997), Marco & Brooks (2003) and Mason et al. (2004), which have been downgraded to the spectral resolution of ∼30. Bottom: Original spectra from Imanishi et al. (1997), Marco & Brooks (2003) and Mason et al. (2004). There is a scaling uncertainty for the profile from Marco & Brooks (2003), see text for details. In both plots we add to the legend the extraction apertures of each work in arcsec. Features at 3.30 μm are due to absorption lines in the calibrator stars and are not to PAHs.

emission artefact appears at 3.3 μm that could be mistaken for the PAH feature at this wavelength (as noted by the original authors). The MATISSE spectra in this figure were calibrated with a late type star (Eta Eridani) that has no Hydrogen absorption features. The overlapping wavelength regions of the calibrated spectra were averaged together, and a continuum determined by a linear fit to the edges of the spectrum. Dividing the original spectra in the vicinity of the carbon lines by the continuum yielded the optical depth spectra included in Fig. 1. The CRIRES spectrum shows the same shape as the earlier, lower spatial resolution spectra, but a somewhat higher optical depth. We do not consider this to be significant: The CRIRES echelle spectroscope was designed to measure very narrow spectral features; it measures 54 separate orders that must be linked together to create the final spectrum and in this process it is possible that some accuracy was lost in the largest scale spectral structure, i.e. that overall depth of the 3.4 μm feature was overestimated.

3 DATA SELECTION

During the commissioning period of a new instrument, it is common to obtain a non-homogeneous set of data quality due to the ongoing optimisation process of the instrument modes and of its related observing procedures. To identify such observations, we had to perform a meticulous data selection processs in several steps, during the pre-reduction and post-reduction stages of the data processing (see Gámez Rosas et al. (2022) for more details). In the first part of this process we corrected the chopping labels of the frames and discarded those that had a chopping frequency different to $\sim 1\,Hz$. After the data reduction we selected sub-observations based on the simultaneous stability of the photometric and interferometric data, using the single dish telescope fluxes (for the photometry) and the root mean squares (RMS) of all frames as points of comparison (for both, the photometric and interferometric data). These methods basically translate to a criterion based on the signal-to-noise of the data.

While comparing sub-observations made a few minutes apart, and using the same BCD setup, either IN-IN or OUT-OUT, we noticed that the baselines defined by the pairs of telescopes UT3-UT4 and UT2-UT4 presented squared visibilities that were much noisier below 3 μm, compared to the same baseline squared visibilities at longer wavelengths. Some sub-observations were actually incompatible in their spectral slope sign, while above 3 μm they had similar shape and behaviour. These were square visibilities with extremely low values (0.002 on average, at 3.3 μm, compared to the lowest values of other baselines which are of ∼0.01), so we decided to also discard these baselines, on the basis that there is no signal at wavelengths that we require to define a continuum. After this selection we recover 18 correlated fluxes from the five different dates. These can be identified by the date of observation and the baseline. We numbered the latter from 0 to 5 depending on the pair of telescopes used (BL=0 uses UT3 and UT4, BL=1 uses UT1 and UT2, BL=2 uses UT1 and UT4, BL=3 uses UT1 and UT3, BL=4 uses UT2 and UT4, and BL = 5 uses UT2 and UT3, in BCD IN-IN) to refer to them in the rest of the paper.

4 THE CONTINUUM

The infrared Spectral Energy Distribution (SED) of an astronomical source in local thermal equilibrium (LTE) gives us information on its temperature, the presence of sources of absorption in front of it (between the source and the observer) and the chemical composition of the latter. Gámez Rosas et al. (2022) used a long and complex procedure to extract SEDs in specific areas over the structures found in their image reconstructions, in L, M and N bands together, and found that their SEDs were best described by two black bodies with a foreground screen of cold dust composed by olivines and carbon, not emitting in the L, M or N bands. In this work we assume a linear continuum and use only the L band correlated flux of each baseline. While using the three MATISSE bands to fit the SEDs resulted in a complete analysis in that work, in our case we can not use the correlated fluxes on the same baseline for the three bands to fit two black bodies since the FOVs at the various wavelengths are different. It was demonstrated in Gámez Rosas et al. (2022) that nearly all the flux in the L band comes from a hot component since the cold dust emission peaks in the N band or at longer wavelengths. Hence, only a small fraction of the cold dust component contributes to (the longer wavelengths of) the L band.

For these reasons, we decided to only use the L band data, and to fit a straight line to the correlated fluxes, and to the average of the single dish photometry obtained from the four UTs. To obtain the correlated fluxes we multiplied the square root of the calibrated square visibilities by the flux-calibrated photometry. Then we defined

the continuum by fitting a straight line at wavelengths: 3.21 to 3.30, and 3.57 to 3.66 μm (using a total of ten data points).

After defining the emission of the continuum for the MATISSE single dish photometry and for the correlated fluxes at each baseline, we subtract it from the data, and normalise the residual correlated fluxes and the residual photometry, dividing by the continuum that we defined for each correlated flux and for the photometry, respectively. We display the features obtained in Fig. 1 for the photometry, and in Fig. 2 for the correlated fluxes. We also display the linear fit on top of the data points in the Annex in Figs A1 and A2. We discuss the shapes of the features in absorption resulted from this process in Section 6.

5 RESULTS

5.1 Single dish spectra

After fitting the continuum, subtracting it from the data, and normalising the residual flux of the MATISSE single dish photometry, as described in Section 4, we see a broad absorption feature with central wavelength $\lambda \simeq 3.45\ \mu m$. In Fig. 1 (top) we show an average of the continuum subtracted and normalised features obtained from the four MATISSE photometries (taken in the different dates of observations) and compare it to the optical depths at different spatial resolutions from Imanishi et al. (1997), Marco & Brooks (2003) and Mason et al. (2004) and our CRIRES data (which correspond to 3.8', 1', 0.48', and 0.2' wide slits, respectively), downgraded to the spectral resolution of our observations and comparing to our own single-dish spectrum, which has an effective FOV of 0.1'. Marco & Brooks (2003) provides a continuum subtracted spectrum in units of flux density, so we had to normalise it and scale it just for comparison purposes, we used a scaling factor of 0.85. In Fig. 1 (bottom) we show the original spectra from Imanishi et al. (1997), Marco & Brooks (2003), Mason et al. (2004) and CRIRES. It is important to remark that the shapes of the resulting absorption profiles obtained by each work might differ slightly depending on the selection of the underlying continuum. In particular, different data points adopted for the edges of the feature where a linear continuum is fit could yield different slopes, therefore changing the shape of the resulting feature. The spectra all show the characteristic double-peaked absorption feature of the C-H stretch lines of aliphatic carbon. There is no strong trend of shape or optical depth with resolution, indicating that the emission and absorption sources are essentially unresolved with the single-dish telescopes. In the CRIRES and MATISSE spectra, there is no indication of any emission near the PAH feature at 3.3 μm. In the other spectra this appears as an artefact of the calibration procedure as explained in Section 2.2.

5.2 MATISSE interferometric data

To further understand the variations of the optical depth at the different baselines we compare the correlated fluxes to the best Gaussian fit of the photometric spectrum. In Fig. 1 (top) we show the Gaussian fitted to the photometry in a dashed black line. The match to a Gaussian profile is outstanding with the peak of the absorption taking place at 3.45 μm. To compare the correlated fluxes we fixed two of the best fit parameters of the photometry: the mean and the stardard deviation. Then we fit the amplitude. This comparison allows us to define an optical depth at 3.45 μm.

In Fig. 2 we show the 18 spectra obtained after subtracting the continuum and normalising the correlated fluxes of the different baselines (blue steady line). We also show the Gaussian obtained from the best fit of the amplitude (grey steady line) inside the $\pm 1\sigma$ fit (light blue shaded area). The latter is given quantitatively for $\lambda = 3.45\ \mu m$ in Table 1 under column $\tau_{3.45\mu m}$, and it is the uncertainty of the peak of the absorption or the optical depth, since only the amplitude of the Gaussian is fit. To calculate the significance of the features, $\sigma_{3.45\,\mu m}$ (black dashed line), we took the standard deviation of the correlated fluxes at the ten wavelengths that we used to fit the continuum. This quantity gives us an idea of the signal to noise ratio of the absorption at $\lambda = 3.45\,\mu m$, based on the variations of the continuum at the edges of the feature. We note that the noise is dominated by the data points at the shortest wavelengths.

In Table 1 we show the optical depths ($\tau_{3.45\mu m}$) with its 1σ confidence interval, and the significance ($\sigma_{3.45\mu m}$) of the features that we find at each baseline. We also add the main parameters that identify the observation and the baseline, like the ID number, day of the observation the number of baseline, and the u and v coordinates, the position angle (PA), and baseline length (BLL).

In Fig. 3 we show the features with their different optical depths and their significance on the *uv*-plane. We use different colors for different optical depths. We see that the absorption is very inhomogeneous across the entire source.

The plots in Fig. 2 represent changes in absolute correlated flux, the literal interpretation of this is somewhat complicated by the nature of the interferometric observations. However, we believe that the shapes shown here represent line absorption only because the shape of the curves correspond to the overall shape of the absorption as seen in the highest resolution single dish measurements, allowing for the fact that there is probably a diffuse absorption feature on larger scales, bringing the whole curve into absorption.

To better understand how the shape of the absorption features vary across the sources we plot the optical depths at 3.45 μm for each baseline against the PA and BLL in Fig. 4. The error bars represent the standard deviation ($\pm 1\sigma$) of the Gaussian fit used to calculate the optical depths. In the case of the MATISSE data used for this work, we can consider the differences between the observations on the uv plane as real for distances larger than the diameter of the UTs, which is 8 m. We take a conservative point of view and filled the markers in Fig. 4 with the same color when the uv-points have a distance shorter than 12 meters. We see quick changes in the optical depths of features across the BLLs and PAs, but in general, we see a decrease in $\tau_{3.45\mu m}$ with a larger PA. There is a hint of the same behaviour with BLL. In conclusion, the MATISSE observations reveal the presence of spatial variations in the absorbing characteristics of the foreground dust as probed by the profiles of the features between 3.3 and 3.6 μm at sub-parsec scales.

6 DISCUSSION

6.1 The 3.4 μm absorption feature in NGC 1068 and other sources

Many galactic sources show either absorption or emission features in the 3 μm region. Absorption spectra are generally dominated by a feature at 3.4 μm with considerable substructure. The profile of this feature is very characteristic for aliphatic hydrocarbon solids – e.g. hydrogenated amorphous carbon (HAC)– consisting of the symmetric and asymmetric CH stretch of methyl (CH_3; 3.47 and 3.38 μm, respectively) and methylene (CH_2; 3.52 and 3.42 μm, respectively) groups (Sandford et al. 1991). The relative strength of these features is a measure of the chain length of the aliphatic groups and the observations reveal the dominance of short chains in interstellar carbon dust, as well as an average $-CH_2-/-CH_3-$ ratio of 2.0–2.5. Subsequent

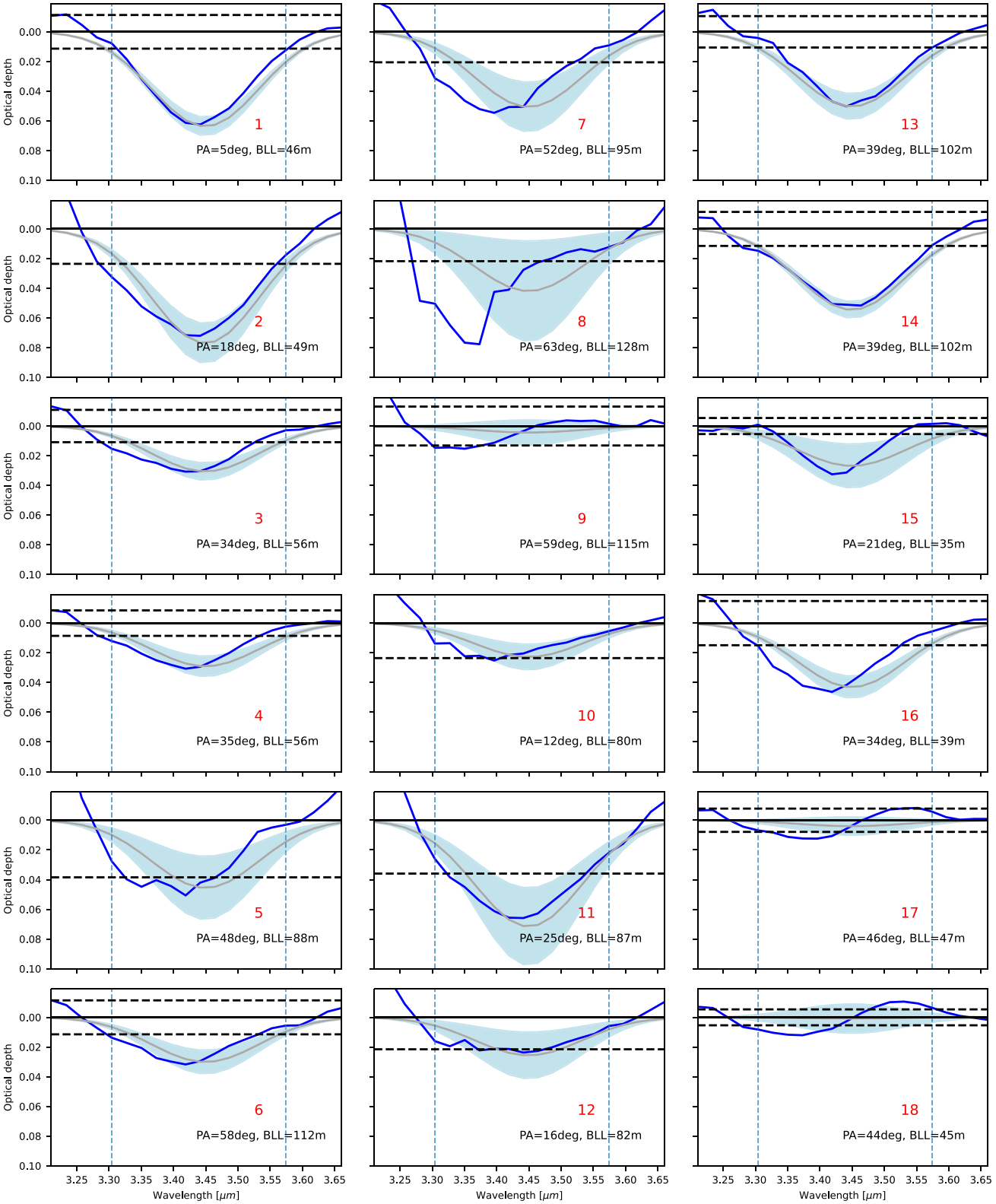

Figure 2. Different continuum subtracted and normalised features obtained at the selected baselines. The small text to the bottom right corner of each profile refers to the ID, PA and BLL. We also show the Gaussian obtained from the best fit of the amplitude (grey steady line) inside the $\pm 1\sigma$ fit (light blue shaded area), and the $\pm\sigma_{3.45\mu m}$ significance level (dashed horizontal lines, see text for details). The vertical dashed lines in blue separate the wavelengths where the continuum was defined, to the shorter and longer wavelengths around the feature.

Table 1. Features at each baseline for all selected observations identified by a number (ID), the observing date (D) and baseline number (BL), D and BL are defined in logic 0. The rest of the columns are the u-coordinate (in units of meters), the v-coordinate (in units of meters), PA (in units of degrees), the BLL (in units of meters), the optical depth at 3.45 μm ($\tau_{3.45\mu m}$) with its 1σ confidence interval, and the significance of the feature at 3.45 μm ($\sigma_{3.45\mu m}$).

ID	D	BL	u	v	PA	BLL	$\tau_{3.45\mu m}$	$\sigma_{3.45\mu m}$
1	0	1	4	46	5	46	0.068 ± 0.007	6.0
2	1	1	15	46	18	49	0.083 ± 0.015	3.5
3	3	1	31	46	34	56	0.033 ± 0.006	3.0
4	4	1	32	46	35	56	0.031 ± 0.007	3.6
5	0	2	66	58	48	88	0.049 ± 0.023	1.3
6	1	2	95	58	58	112	0.032 ± 0.009	2.8
7	2	2	75	58	52	95	0.054 ± 0.018	2.6
8	3	2	114	59	63	128	0.045 ± 0.037	2.1
9	4	2	99	59	59	115	0.005 ± 0.009	0.4
10	0	3	16	79	12	80	0.024 ± 0.009	1.0
11	1	3	37	79	25	87	0.077 ± 0.028	2.1
12	2	3	23	79	16	82	0.027 ± 0.017	1.3
13	3	3	65	79	39	102	0.054 ± 0.009	5.1
14	4	3	64	79	39	102	0.058 ± 0.006	5.1
15	0	5	12	32	21	35	0.029 ± 0.016	5.3
16	1	5	22	32	34	39	0.046 ± 0.008	3.1
17	3	5	33	32	46	47	0.004 ± 0.007	0.5
18	4	5	32	32	44	45	0.001 ± 0.011	0.2

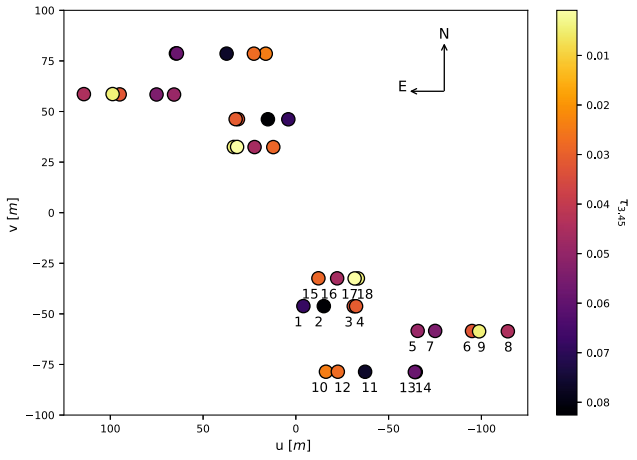

Figure 3. Distribution of the observed uv-points color-coded by optical depth of the features, so, $\tau_{3.45\mu m}$ from Table 1. The numbers below the coloured circles refer to the ID number of each uv-point as in Table 1.

studies revealed the widespread presence of this feature in the diffuse ISM of the Milky Way with little spectral variation (Sandford et al. 1991; Pendleton et al. 1994; Chiar et al. 2000). In addition to the 3.4 μm feature, ISO spectra revealed a weak absorption feature at 3.3 μm due to the CH stretching mode in aromatic materials (Chiar et al. 2000; Hensley & Draine 2021). While in the ISM these dust features are seen in absorption, they are in emission in some post AGB objects, like IRAS 05341 + 0852 (Joblin et al. 1996).

The first extragalactic observation of the 3.4 μm absorption feature was done toward NGC 1068 (Bridger, Wright & Geballe 1994). Since then, this feature has been studied with a variety of instruments at different spatial and spectral resolutions (See Fig. 1). High spectral resolution observations reveal sub peaks at 3.38, 3.42, and 3.48 μm. The profile of the 3.4 μm feature in NGC 1068 resembles closely the 3.4 μm feature observed toward the galactic centre in our own Galaxy (Dartois et al. 2004; Tomono et al. 2006; Geballe et al. 2009).

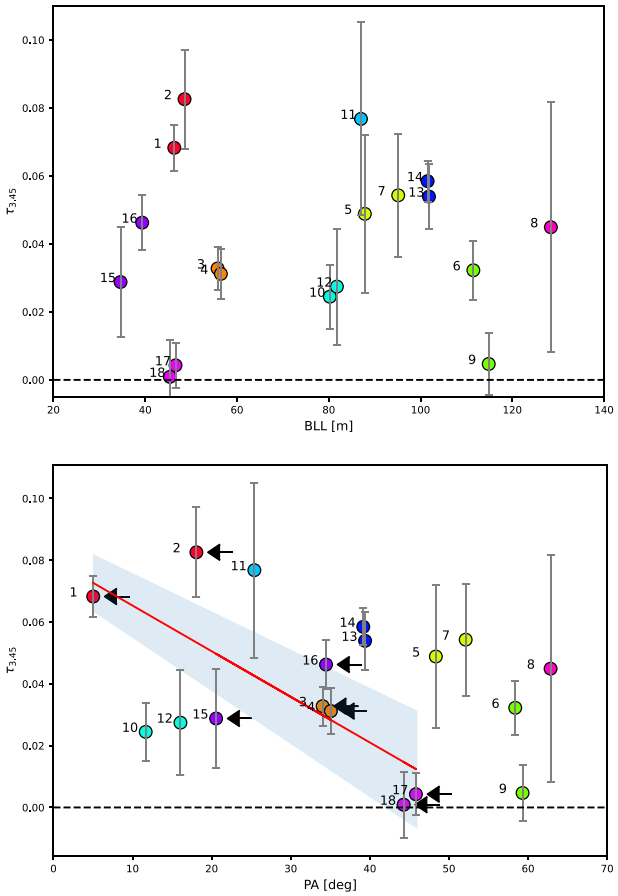

Figure 4. Optical depth at 3.45 μm ($\tau_{3.45\mu m}$) with baseline length (BLL, top) and position angle (PA, bottom). Markers with the same color indicate uv-points that are close by, see text for details. The numbers to the left of the coloured circles refer to the ID number of each uv-point as in Table 1. The red line shows a linear fit to the shortest baseline data points indicated by arrows and the shaded region shows the $\pm 1\sigma$ confidence interval of the fit (see Section 6.2 for details).

This feature has now been seen in a variety of extragalactic nuclei, including Seyferts and (U)LIRGS (Imanishi 2000; Mason et al. 2004; Imanishi et al. 2006; Dartois et al. 2007). The similarity in the profiles points towards a common carrier.

We argue that the feature detected by MATISSE in both the single dish spectra and in the correlated fluxes can be explained by this same absorption caused by aliphatic hydrocarbons that has been identified in spectra with higher spectral resolution and lower angular resolution. We have filled up the range of apertures used for different observations down to the slit size that we used with MATISSE (single dish photometry) by comparing to a new CRIRES spectrum. The CRIRES spectrum has clear signatures of the 3.4 μm feature reported in the literature. The feature is consistent with the spectra shown by Mason et al. (2004) and Marco & Brooks (2003).

In the case of the correlated fluxes, we obtain a good fit with the scaled Gaussians that aim to mimic the absorption feature of the MATISSE photometry with varying optical depths (see Section 5). Indeed, only baselines 7 and 8 leave out of the fitted Gaussian a large area outside the light blue area. This area looks like a bump towards the short wavelengths. Actually, in most baselines it is evident a small shift of the data to the left of the fitted Gaussian. Since this shift is smaller than our spectral resolution ($\Delta\lambda \sim 0.11\,\mu m$) we

think that it does not come from any astrophysical phenomena and that this is rather inside the uncertainty of the data. With enough spectral resolution, a shift in a feature could be caused by blending of other features or by an ambiguous definition of the continuum by the presence of other features, causing an apparent different slope of the continuum. In the case of the aliphatic hydrocarbons, it has been seen in other sources accompanied by a PAH feature at 3.3 μm in absorption or in emission. This is not the case for NGC 1068, at least not in emission. Our single dish spectrum does not show any signs of emission at those wavelengths, and neither in absorption. In the case of the interferometric data, the feature in absorption would have to be extremely weak for it to not to be shown in the photometry. But having these small excesses in both wings of the features (and not only at the wavelength where the PAHs can be seen) argues in favour of a glitch by the data. Only baselines 7 and 8 could present a case for a possible PAH feature in absorption (one detail here is that baseline 7 does coincide with baseline 5 on showing the same bump at 3.3 μm). But we find it unlikely when comparing to the features observed in the diffuse ISM (Chiar et al. 2013) since the aromatic component presents a small fraction of about a quarter of the optical depth at the peak of the aliphatic hydrocarbon absorption feature. While baselines 5 and 7 account for about half of the optical depth at 3.3 μm, baseline 8 presents a bump with an optical depth about a factor of 2 larger at 3.3 μm. Future observations with higher spectral resolution will be needed to resolve this question.

6.2 Interpretation

Using a conservative approach, we take as real changes in the optical depth in uv-points separated by more than 12 m. In Fig. 4 we can see that most sets of data points with matching colours coincide within their error bars. We see a problem with points 6 and 9 (not agreeing with each other) and with 16, which does not agree with 17 and 18. From the cluster of points (*1,2,3,4,15,16*) we see significant changes in opacity corresponding to changes in uv-position of ∼20 meters. The geometry of fringe forming shows that changes on *small* scales in the uv-plane correspond to changes on *large* scales on the sky; a change on a uv-scale of Δu implies a significant change in the optical depth structure on scales of $\Delta\theta \sim \lambda/3\Delta u$ radians, which in this case corresponds to ∼20 milliarcsec, for the wavelength $\lambda \sim 3\,\mu m$. This is the approximate size of the bright central 3 μm continuum emission seen in Gámez Rosas et al. (2022). Thus while at this point we cannot create a true image of the distribution of the foreground layer absorbing L-band photons, we can conclude that it must vary significantly across the whole emission feature seen in Gámez Rosas et al. (2022), on scales ranging from 3–20 milliarcsec or 0.2–1.4 parsec at the distance of NGC 1068.

There is some indication in Fig. 3 that the uv-points with the highest optical depth align near the North-South axis especially those at shorter baselines. To test this, we have plotted optical depth versus position angle in Fig. 4, with the shortest baselines (BLL<60 m: those with IDs: 1,2,3,4,15,16,17 and 18) marked by black arrows. These points show a strong increase in $\tau_{3.45\mu m}$ as the position angle approaches North; the drawn red line shows a linear fit to this trend inside the $\pm 1\sigma$ confidence interval (blues shaded area). Fitting a horizontal line to these data points fails to a 6σ level. The longer baselines do not show this effect. This increase of $\tau_{3.45\mu m}$ on short baseline uv-points towards this direction suggests that the Carbon absorption can be viewed as an elongated structure at this position angle.

This position angle is actually close to the direction at which the inner radio jet is being launched (almost North-South, see Gallimore, Baum & O'Dea (2004)), and to the regions of the center of the ionization cone, which is calculated to be ∼10 degrees based on Hubble Space Telescope images (Raban et al. (2009), López-Gonzaga et al. (2014)). In any case, what Figs 3 and 4 are telling us is that the variations of the densities of the foreground layer absorbing the L band photons are taking place on sub-pc scales. If we consider a system of clumps of dust forming the torus, we actually have a function of temperatures of the dust with distance. As we observe with a limited spatial resolution two temperatures tend to dominate that reflect averages of the hottest and the coldest emitting dust. These average temperatures depend on the optical depth functions with radii (Nenkova et al. 2008). Gámez Rosas et al. (2022) finds that the **absorbing** foreground screen of dust responsible for the peculiar shape of the 9.7 μm feature is made of amorphous olivines with a size of 0.1 μm at least 10 to 15 pc away from the AGN. This is considerably farther along the line of sight from the center than the warmer emitting dust, and in order to be in absorption the foreground dust must be considerably colder than the emitting dust. Similarly, the aliphatic foreground dust temperature must be lower than the hot central continuum emitting dust (450 to ∼1400 K) to show the feature in absorption, and must be considerably farther away, perhaps at the distance of the olivine absorbing material. Thus we find that the aliphatic material changes optical depth on small spatial scales, 0.3–2 parsec, that are probably considerably smaller than than their distance from the AGN, which is consistent with the 'clumpy torus' model of AGN obscuration.

According to Table 1 in Gámez Rosas et al. (2022), we see that the large range of filling factors (0.04–1.0) that correspond to the cold components with temperatures between 180 K and 500 K allow for the possibility to have windows where the emission is not absorbed until reaching the dust with temperatures lower than 150 K. It is crucial to constrain the composition and distribution of the absorbing dust in the foreground to derive the right shape of the SEDs. Gámez Rosas et al. (2022) proved that adding 0.1 μm carbon grains in a mix with up to 20 per cent of carbon in weight made the temperatures of the hot component to oscillate from +50 to almost + 500 K using the highest content of carbon.

In conclusion, we agree with the addition of the carbon grains to the opacities of the absorbing dust in Gámez Rosas et al. (2022). Nevertheless, a more detailed analysis to define the right proportion of carbon/olivines is needed starting by higher resolution spectra and linking the SEDs from L to N bands, to be able to differ the contribution from both dust species accurately.

6.3 Carbon abundance

We calculate the column density $N_{3.4}$ of the carbon locked up in the hydrocarbon material along the line of sight following the methodology of Günay et al. (2018):

$$N_{3.4} = \frac{\int \tau_{3.4}(\bar{\nu}) d\bar{\nu}}{A} \quad (1)$$

where $\bar{\nu}$ is the measured frequency (in cm^{-1}) and A is the integrated carbon absorption coefficient, whose value reported by Günay et al. (2018) is $A = 4.69 \times 10^{-18}$ cm group^{-1} based on laboratory measurements of aliphatic **Interstellar Dust Analogues** (ISDAs) generated by exposure of acetylene gas to a plasma arc. From the MATISSE absorption profiles the value of the integral of the line is 10 cm^{-1}, we obtain $N_{3.4} = 2.1 \times 10^{18} cm^{-2}$

Comparing to an average over the areas with L band emission, of the dust surface density of the olivines + carbon reported in Gámez Rosas et al. (2022), we find $N_{9.7(average)} = 296 - 542\,\mu g\,cm^{-2}$,

converting $N_{3.4}$ to the same units we obtain: $N_{3.4}/N_{9.7(average)} \sim 2.0 - 3.6$ per cent, which is the range of mass ratios of the abundances of carbon in the aliphatic form to the dust grains made of carbon and olivines. This is consistent with the values of 2.6 ± 0.05 per cent reported in Sandford et al. (1991) for several lines of sight of the diffuse ISM in our Galaxy.

7 CONCLUSIONS

In this work we analyse the features found in the MATISSE L-band single dish spectrum and correlated fluxes of the Seyfert 2 NGC 1068. The single dish spectrum shows a broad absorption feature that has been observed before at lower spatial resolutions, resembling the 3.4 μm aliphatic hydrocarbon feature seen in the diffuse ISM. We also find broad absorption lines with a significance larger or equal to $1\sigma_{3.45\mu m}$ in 15 of the 18 correlated flux spectra. The latter vary in optical depth with distance and direction with respect to the photo-centre. We also present a new CRIRES spectrum that links the apertures used by previous single-dish observations to the one of MATISSE.

We conclude:

(i) The 3.4 μm absorption in the MATISSE single-dish spectrum of NGC 1068 is caused by aliphatic hydrocarbons

(ii) The average column density of aliphatic carbon derived from the spectrum is $\sim 2.0 \times 10^{18}$ cm $^{-2}$ and the mass ratio of carbonaceous to silicate olivine dust is $\sim 2 - 3.6$ per cent, in accordance to several lines of sight of the diffuse ISM in our Galaxy (Sandford et al. 1991).

(iii) The 3.4 μm absorption features in the interferometric MATISSE correlated fluxes of NGC 1068 are also caused by aliphatic hydrocarbons. Their optical depths vary over scales of 0.2–1.4 parsec in the plane of the sky, although probably placed at a larger distance from the AGN along the line of sight. This is consistent with the clumpy torus model.

(iv) Based on the observed trend of the larger optical depths with small position angles of the shortest baselines, the absorption seems to peak in the extended emitting areas towards the direction of the inner radio jet and close to the center of the ionization cone.

(v) There is no indication in either the single dish CRIRES, MATISSE, or the high spatial resolution MATISSE interferometric spectra for 3.3 μm emission from PAHs. These are presumably destroyed by the UV- and X-radiation from the AGN.

ACKNOWLEDGEMENTS

In memory of our colleague Klaus Meisenheimer, who was integral to the MATISSE project's beginnings and shared cherished moments with us. His influence continues to inspire our work. The use of the data for this work has been approved by ESO and, complying with ESO policy, it has been released in the public archive. The observations were collected at the European Southern Observatory under ESO programmes 60.A-9257 (commissioning) and 0104.B-0322(A) (MATISSE Guaranteed Time Observations of AGNs). The CRIRES observations were taken in open time under ESO proposal 108.223N. V.G.R. was partially supported by the Netherlands Organisation for Scientific Research (NWO). J.H.L. acknowledges the support of the French government through the UCA JEDI Investment in the Future project managed by the National Research Agency (ANR) under the reference number ANR-15-IDEX-01. W.J. was supported in part by the Netherlands Algemeen Burgerlijk Pensionfonds (ABP).

DATA AVAILABILITY

The raw data underlying this article were accessed from ESO at http://archive.eso.org/eso/eso_archive_main.html under programs 60.A-9257 (commissioning) and 0104.B-0322(A) for MATISSE, and 108.223N for CRIRES. The derived data generated in this research will be shared on reasonable request to the corresponding author. The reduced and calibrated data underlying this article are available in https://github.com/VioletaGamez/NGC1068_MATISSE, at https://doi.org/10.5281/zenodo.5599363.

REFERENCES

Bridger A., Wright G. S., Geballe T. R., 1994, in Infrared Astronomy with Arrays: The Next Generation, McLean I. S.ed., Astrophysics and Space Science Library Vol. 190, Astronomy with Arrays, . p. 537
Chiar J. E., Pendleton Y. J., Geballe T. R., Tielens A. G. G. M., 1998, ApJ, 507, 281
Chiar J. E., Tielens A. G. G. M., Whittet D. C. B., Schutte W. A., Boogert i. C. A., Lutz D., van Dishoeck E. F., Bernstein M. P., 2000, ApJ, 537, 749
Chiar J. E., Adamson A. J., Pendleton Y. J., Whittet D. C. B., Caldwell D. A., Gibb E. L., 2002, ApJ, 570, 198
Chiar J. E. et al., 2006, ApJ, 651, 268
Chiar J. E., Tielens A. G. G. M., Adamson A. J., Ricca A., 2013, ApJ, 770, 78
Chiar J. E., de Barros A. L. F., Mattioda A. L., Ricca A., 2021, ApJ, 908, 239
Cohen R. D., Rudy R. J., Puetter R. C., Ake T. B., Foltz C. B., 1986, ApJ, 311, 135
Cruzalebes P. et al., 2019, MNRAS, 490, 3158
Dartois E., Marco O., Muñoz-Caro G. M., Brooks K., Deboffle D., d'Hendecourt L., 2004, A&A, 423, 549
Dartois E. et al., 2007, A&A, 463, 635
Ehrenfreund P., Robert F., D'Hendecourt L., Behar F., 1991, A&A, 252, 712
Gallimore J. F., Baum S. A., O'Dea C. P., 2004, ApJ, 613, 794
Gámez Rosas V. et al., 2022, Nature, 602, 403
Geballe T. R., Mason R. E., Rodríguez-Ardila A., Axon D. J., 2009, ApJ, 701, 1710
Günay B., Schmidt T. W., Burton M. G., Afşar M., Krechkivska O., Nauta K., Kable S. H., Rawal A., 2018, MNRAS, 479, 4336
Günay B., Burton M. G., Afşar M., Schmidt T. W., 2020, MNRAS, 493, 1109
Hensley B. S., Draine B. T., 2021, ApJ, 906, 73
Imanishi M., 2000, MNRAS, 313, 165
Imanishi M., Terada H., Sugiyama K., Motohara K., Goto M., Maihara T., 1997, PASJ, 49, 69
Imanishi M., Dudley C. C., Maloney P. R., 2006, ApJ, 637, 114
Jaffe W. et al., 2004, Nature, 429, 47
Joblin C., Tielens A. G. G. M., Allamandola L. J., Geballe T. R., 1996, ApJ, 458, 610
López-Gonzaga N., Jaffe W., Burtscher L., Tristram K. R. W., Meisenheimer K., 2014, Astron. Astrophys., 565, A71
Lopez B. et al., 2014, The Messenger, 157, 5
Lopez B. et al., 2022, A&A,, 659, A192
Marco O., Brooks K. J., 2003, A&A, 398, 101
Mason R. E., Wright G., Pendleton Y., Adamson A., 2004, ApJ, 613, 770
Nenkova M., Sirocky M. M., Ivezić Ž., Elitzur M., 2008, Astrophys. J., 685, 147
Pendleton Y. J., Allamandola L. J., 2002, ApJS, 138, 75
Pendleton Y. J., Sandford S. A., Allamandola L. J., Tielens A. G. G. M., Sellgren K., 1994, ApJ, 437, 683
Petrov R. G. et al., 2022, MATISSE Instrument Performance Report: Commissioning Report V2.0, Research Report Version 2.0, European Southern Observatoryhttps://hal.archives-ouvertes.fr/hal-03763766
Raban D., Jaffe W., Röttgering H., Meisenheimer K., Tristram K. R. W., 2009, MNRAS, 394, 1325
Sandford S. A., Allamandola L. J., Tielens A. G. G. M., Sellgren K., Tapia M., Pendleton Y., 1991, ApJ, 371, 607
Tomono D., Doi Y., Usuda T., Nishimura T., 2001, ApJ, 557, 637
Tomono D., Terada H., Kobayashi N., 2006, ApJ, 646, 774

APPENDIX A: TABLE OF MATISSE OBSERVATIONS AND LINEAR FITS

Table A1. Observing log for NGC 1068 L and M band observations and the associated calibrators. Columns: under Exposure we list the date and time (UT) of the exposure start, which can be used to access the data in the ESO Archive. Under the column Target we list the target names and for calibrator stars their spectral type, diameter (milliarcsec) and their fluxes in Janskys for [L-, and M- bands]. τ_0 gives the V-band atmospheric correlation time (msec) which characterizes atmospheric stability. Day gives the code for D that is used in Table 1.

Exposure	Target	τ_0	Comments	Day
2018-09-22T04:27:12(LM) 2018-09-22T04:31:37(LM)	NGC 1068	5.2		0
2018-09-22T04:56:13(LM) 2018-09-22T04:57:54(LM) 2018-09-22T04:59:20(LM) 2018-09-22T05:00:46(LM) 2018-09-22T05:02:21(LM) 2018-09-22T05:03:47(LM) 2018-09-22T05:05:13(LM) 2018-09-22T05:06:38(LM)	HD 16658 K0III 0.27 mas [1.09, 0.59]	4.6	Calibrator for preceding Observation	
2018-09-25T08:21:57(LM) 2018-09-25T08:22:59(LM) 2018-09-25T08:24:00(LM) 2018-09-25T08:25:11(LM) 2018-09-25T08:26:12(LM) 2018-09-25T08:27:13(LM) 2018-09-25T08:28:15(LM)	HD 20356 K4III 1.63 mas [25.8, 15.1]	6.8	Calibrator for preceding Observation	
2018-09-25T05:36:10(LM) 2018-09-25T05:41:06(LM)	NGC 1068	4.9	UT2 visibilities flagged	1
2018-09-25T02:51:31(LM) 2018-09-25T02:52:45(LM) 2018-09-25T02:53:44(LM) 2018-09-25T02:54:42(LM) 2018-09-25T02:55:51(LM) 2018-09-25T02:56:51(LM) 2018-09-25T02:57:49(LM) 2018-09-25T02:58:48(LM)	HD 209240 K0III 0.74 mas [8.3, 5.7]	4.0	Calibrator of preceding Observation	
2019-11-07T01:51:29(LM) 2019-11-07T01:56:46(LM)	NGC 1068	3.1	Telescope UT2 failed	2
2019-11-07T05:50:50(LM) 2019-11-07T05:56:08(LM)	NGC 1068	7.4		3
2019-11-07T07:15:58(LM) 2019-11-07T07:21:15(LM)	NGC 1068	7.3		4
2019-11-07T07:45:30(LM) 2019-11-07T07:46:47(LM) 2019-11-07T07:48:07(LM) 2019-11-07T07:49:24(LM) 2019-11-07T07:50:50(LM) 2019-11-07T07:52:05(LM) 2019-11-07T07:53:24(LM) 2019-11-07T07:54:44(LM)	HD 18322 Eta Eridani K1IIIb 2.6 [74.1, 44.1]	6.9	Cohen Calibrator Calibrator for all 2019 Observations	

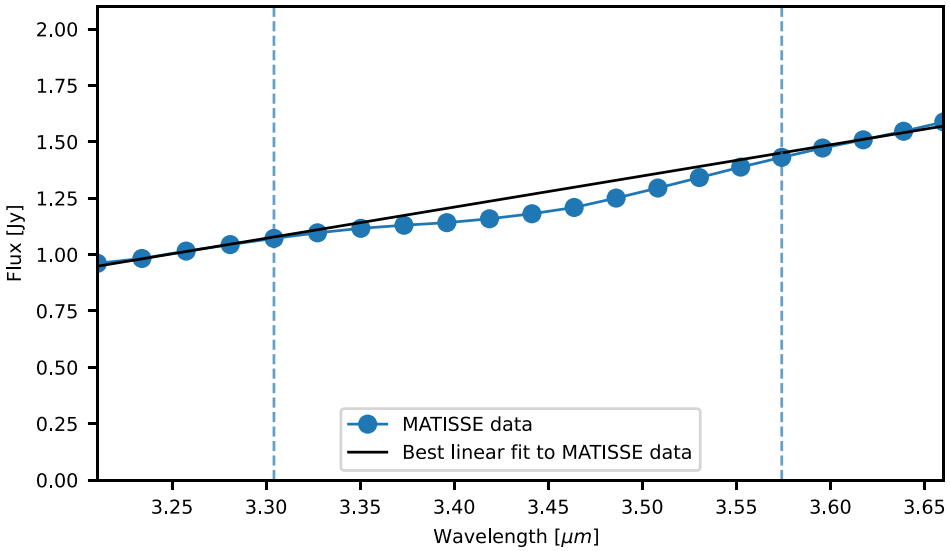

Figure A1. Best linear fit to the MATISSE single dish photometry. The vertical dashed lines in blue separate the wavelengths where the line was fitted around the feature.

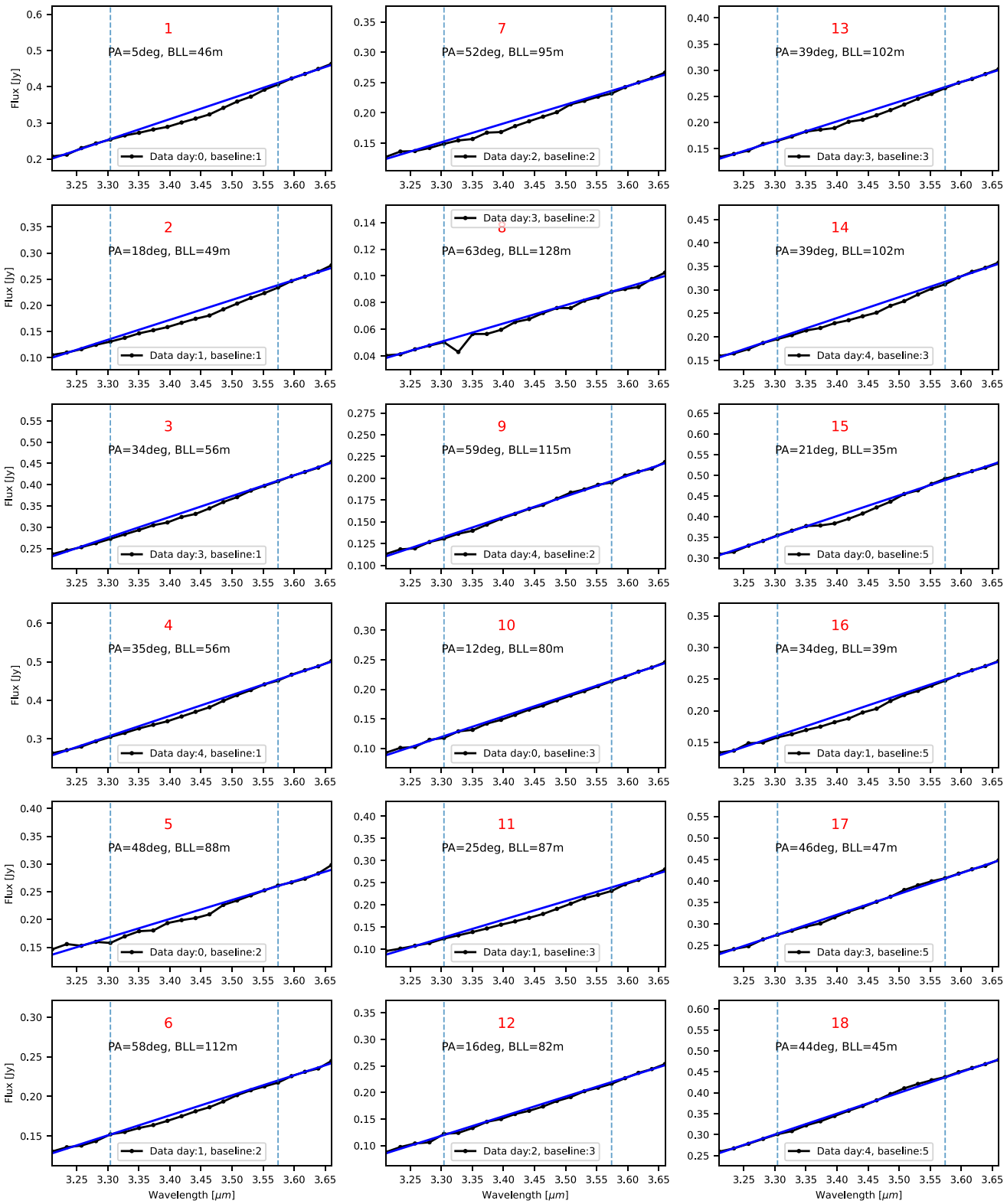

Figure A2. Correlated fluxes at the different baselines with the linear fit to be used as continuum. The small text to the top left of each spectrum refers to the number to identify each baseline in Table 1, and its PA and BLL. The vertical dashed lines in blue separate the wavelengths where the line was fitted around the feature.

This paper has been typeset from a TEX/LATEX file prepared by the author.